J. Bonse, S. Höhm, M. Hartelt, D. Spaltmann, S. Pentzien, R. Koter, S. Marschner, A. Rosenfeld, and J. Krüger

7 Femtosecond laser-induced surface nanostructures for tribological applications

Abstract: Laser-induced periodic surface structures (LIPSS) were generated on two types of steel (100Cr6, X30CrMoN15-1) and two types of titanium (Ti, Ti6Al4V) surfaces upon irradiation with multiple linear polarized femtosecond laser pulses in air environment (pulse duration 30 fs, central wavelength 790 nm, pulse repetition rate 1 kHz, Gaussian beam shape). The conditions (laser fluence, spatial spot overlap) were optimized in a sample-scanning geometry for the processing of large surface areas covered homogeneously by two different types of LIPSS – either near wavelength or sub-100 nm structures. The tribological performance of the nanostructured surfaces was characterized under reciprocating sliding at 1 Hz against a ball of hardened steel using different lubricants and normal forces. After 1000 cycles the corresponding wear tracks were characterized by optical and scanning electron microscopy. For specific conditions, the wear was strongly reduced and the laser-generated nanostructures endured the tribological treatment. Simultaneously, a significant reduction of the friction coefficient was observed in the laser-irradiated LIPSS-covered areas, indicating the benefit of laser surface structuring for tribological applications. The spatially Gaussian shaped beam used for the laser processing was transformed via beam shaping into a top hat distribution at the surface of the samples for optimization. The tribological performance of the laser-induced nanostructures is discussed on the basis of different physical and chemical mechanisms.

7.1 Introduction

Since the first observation of *laser-induced periodic surface structures* (LIPSS), also termed *ripples*, on semiconductors by Birnbaum [1], such structures have been found on almost every material. The generation of LIPSS on laser irradiation is a universal phenomenon [2], although their occurrence, structural size, and formation mechanism depend on the material and irradiation parameters. LIPSS have attracted remarkable interest over the past decades, as their generation is possible in a single-process step. This provides a simple way of surface nanostructuring towards a control of optical, mechanical, or chemical surface properties [3].

7.1.1 Femtosecond laser-induced periodic surface structures (fs-LIPSS)

Since the turn of the new millennium, a remarkable amount of research has been devoted to the formation mechanisms of LIPSS after irradiation by ultrashort laser pulses (see [4–10] and references therein). Typically, two distinct types of LIPSS are observed on irradiation of solids with linearly polarized fs-laser pulses. For strongly absorbing materials (metals and semiconductors) so-called *low-spatial-frequency LIPSS* (LSFL) are observed with a period Λ_{LSFL} close to the irradiation wavelength λ and an orientation perpendicular to the laser beam polarization [11–14]. It is generally accepted that these LSFL are generated by interaction of the incident laser beam with a surface electromagnetic wave (SEW) generated at the rough surface [5, 14–16].

The second LIPSS type are the so-called *high-spatial-frequency LIPSS* (HSFL). With periods Λ_{HSFL} significantly smaller than the incident wavelength, these structures are observed predominantly for laser pulse durations in the fs- to ps-range. Their origin is still discussed controversially in the literature. Second harmonic generation [11, 17], the involvement of specific types of plasmon modes [18–20] or self-organization [4] have been proposed as possible formation mechanisms.

7.1.2 fs-LIPSS on metals

Several groups have already studied the generation of fs-LIPSS on metals [3, 13, 21, 22]. Steel and titanium belong to the most relevant materials used in industrial applications involving tribological demands. Using Ti:sapphire laser pulses, on steel LSFL were mostly reported with spatial periods in the range of 500–700 nm [3, 22–25]. Titanium and its alloys provide high corrosion and temperature resistance along with an extraordinary strength-to-weight ratio, which makes it interesting for many industrial, aeronautical or medical applications. Near-infrared fs-laser processing experiments on titanium revealed both types of LIPSS with LSFL periods between 400 and 800 nm, and HSFL periods of 65 to 95 nm only (for a literature survey refer to Table 1 in [26]).

7.1.3 Technical applications of LIPSS

Different technical applications of LIPSS have recently been proposed and studied, such as surface colorization [21, 22], control of surface wetting behavior [27] or friction management [28–36]. However, the tribological methods and specific test conditions vary strongly among the latter studies, thereby complicating a direct comparison of the results. Mizuno et al. used an atomic force microscopic technique under controlled atmospheric conditions. They reported a reduction of the friction coefficient of fs-LIPSS covered diamond-like-carbon (DLC) films for low normal loads in the nN range [28]. Later, the same group used a ball-on-disk friction test for study-

ing the influence of additional overlayers and hardcoatings, and by complementary geometrical surface patterns [29, 30]. Pfeiffer and co-workers qualified the friction and wear behavior of fs-LIPSS on super-hard tetrahedral amorphous carbon films [31]. Employing a pin-on-disk tribometer under unlubricated conditions, they also found a significant reduction of the friction coefficient and the corresponding wear rate. Eichstädt et al. used a tribometer with a linear reciprocating module in a ball-on-flat configuration. This group presented results of an increased friction coefficient of fs-LIPSS covered silicon for normal loads in the mN range [32]. Chen et al. demonstrated the low friction characteristics of fs-LIPSS-covered microscale stripes on silicon carbide seals in air and water contact by using a ring-on-disk tribometer [33].

In the following chapter, the tribological characteristics of large area fs-LIPSS covered surfaces are systematically qualified. They are compared for four different metals in two different lubricating oils under identical conditions. These results were already partly reported in [34] and [36].

7.2 Experimental details

7.2.1 Materials

Commercial grade-1 titanium (Ti, 99.5 % purity, DIN 3.7025) and grade-5 titanium alloy (Ti6Al4V, DIN 3.7165) were purchased from Schumacher Titan GmbH (Solingen, Germany) as 25 mm diameter rods. These rods were cut into circular slabs of 8 mm thickness and mechanically polished, resulting in mirror-like surface finish with an average roughness $R_a < 10$ nm. Cylindrical slabs of hardened 100Cr6 steel were supplied by Optimol Instruments Prüftechnik GmbH (München, Germany) with 24 mm diameter, 8 mm thickness (DIN 1.3505) and a polished surface ($R_a \sim 35$ nm). Similar sized slabs were acquired from Energietechnik Essen GmbH (Essen, Germany), made of a hardened, nitrogen enriched, high toughness bearing steel (X30CrMoN15-1, DIN 1.4108) with a lapped surface ($R_a \sim 190$ nm).

7.2.2 Laser processing technology

A Ti:sapphire laser amplifier system (Femtolasers, Compact Pro) was used to generate linearly polarized laser pulses of $\tau = 30$ fs duration and $\lambda = 790$ nm central wavelength at a pulse repetition rate of $f = 1$ kHz. The laser pulse energies E were measured with a pyroelectric detector. The pulses were focused by a spherical dielectric mirror (500 mm focal length).

The samples were mounted on a motorized x-y-z linear translation stage and placed normal to the incident laser beam a few millimeters in front of the geometrical laser focus. At this sample position, a Gaussian-like beam profile was measured

with a radius $w_0(1/e^2) \sim 140\,\mu m$. The corresponding peak fluence in front of the sample surface was calculated via $\phi_0 = 2E/(\pi w_0^2)$ [37]. The sample was moved in a meandering motion under the focused laser beam at a constant scan velocity v_x and with a line offset of Δy. This led to the processing of a square-shaped area of $5 \times 5\,mm^2$. Under these conditions, the effective number of laser pulses per focused laser spot diameter $D = 2w_0$ (for a single laser processing pass) accounts in the x-direction to $N_{eff} = (D \times f)/v_x$ [37]. In some cases, an additional pass with identical processing parameters was performed at the same sample area. Subsequent to laser processing in ambient air, the samples were cleaned in acetone for five minutes using an ultrasonic bath and stored in a desiccator to avoid long-term chemical reactions with the ambient air atmosphere.

7.2.3 Sample characterization

The laser-processed surface regions were characterized by optical microscopy (OM, Nikon Eclipse L200), white light interference microscopy (WLIM, Zygo NewView 5020), and scanning electron microscopy (SEM, Carl Zeiss Gemini Supra 40).

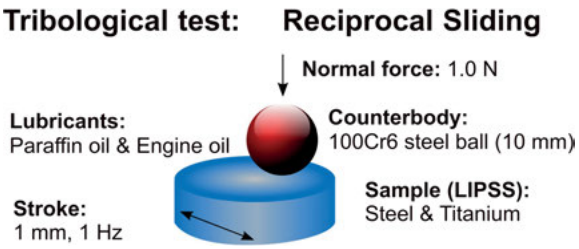

Fig. 7.1: Scheme of the reciprocal sliding tribological test (RSTT).

Reciprocal sliding tribological tests (RSTT) were performed in a home-made tribometer by sliding the laser-processed samples at a normal force of $F_N = 1.0\,N$ against a hardened and polished steel ball (100Cr6, 10 mm diameter, $R_a \sim 6\,nm$) as counterbody (see the scheme in Fig. 7.1). The velocity between sample and ball is a sine function with its maximum value in the middle of the stroke distance of 1 mm total length. During the movement, the frictional forces acting on the sample are recorded. From this information and the known normal force, the friction coefficient can be quantified [38]. A 100Cr6 ball as counterbody is our "standard" in RSTT and allows comparison with previous experiments.

The radius of the ball-sample contact was estimated using a Hertzian deformation model (HDM) of a sphere in contact with a flat sample. At this normal force, the contact radius lies between 30 and 40 µm for all materials tested, i.e., it is about 2–3 orders of magnitude larger than the LIPSS periods. Moreover, for the given conditions, the HDM predicts material (hardness) dependent sample-ball deformations between 200

and 300 nm, i.e., values of the order of the expected modulation depths of the LSFL (see Section 7.3.1). In previous studies [39, 40] it was shown that RSTT experiments with balls of 10 mm diameter and normal forces between 0.1 and 1.0 N are sensitive to surface grooves with a depth of ~ 160 nm and widths down to 100 nm only, i.e., groove widths of less than 1/500 of the Hertzian diameter of the contact area [40]. In the RSTT experiments, 1000 cycles were performed at a frequency of 1 Hz in a synthetic paraffin oil (free of additives) as well as in a fully formulated engine oil with additives (Castrol VP-1). The range of uncertainty in the friction coefficient measurements is ± 0.02. After the tribological tests, the samples were cleaned in petroleum ether for five minutes using an ultrasonic bath in order to remove the residual lubricants. Subsequently, the corresponding wear tracks were inspected by OM and SEM.

7.3 Tribological performance of LIPSS

In a first step, suitable laser processing conditions were identified and optimized for the generation of large surface areas (several tens of mm^2) covered homogeneously by LIPSS on all four metals (Ti, Ti6Al4V, 100Cr6, X30CrMoN15-1). As an example, Section 7.3.1 presents the optimized processing conditions for the titanium alloy covered by near-wavelength (LSFL) and sub-100 nm LIPSS (HSFL), both generated with a spatial Gaussian beam profile. In a second step, the tribological performance of the different types of LIPSS was systematically tested for all materials in the two different lubricating oils – exemplified for LSFL and HSFL in Section 7.3.2. The process optimization is demonstrated in Section 7.3.3. Here, spatial beam shaping is used to transform the Gaussian beam into a top hat distribution.

7.3.1 Large area surface processing of LIPSS

By choosing a peak fluence of $\phi_0 = 0.11\ J/cm^2$, a scan velocity of $v_x = 5$ mm/s ($N_{eff} \sim 56$) and a line offset of $\Delta y = 0.1$ mm at the given focusing conditions, a common set of parameters was identified which allowed the generation of LSFL structures on all four different metals with a single laser processing pass [34, 36]. As an example, Fig. 7.2 (a) shows the WLIM topography of the central $1.40 \times 1.05\ mm^2$ laser processed surface area in a 3D view (left). The periodic pattern observed here is formed by the arrangement of adjacent ablation lines. A cross-sectional surface line profile is given below the corresponding topography and reveals comb-like height variations of $\Delta z = \pm 150$ nm. Note that the spatial resolution of the WLIM is not sufficient here to resolve the LSFL. Scanning electron microscopy confirmed the simultaneous existence of the LSFL at the top and bottom of the surface topography [36]. As seen on the right hand side of Fig. 7.2 (a), LSFL are formed with periodicities of (620 ± 80) nm and an orientation

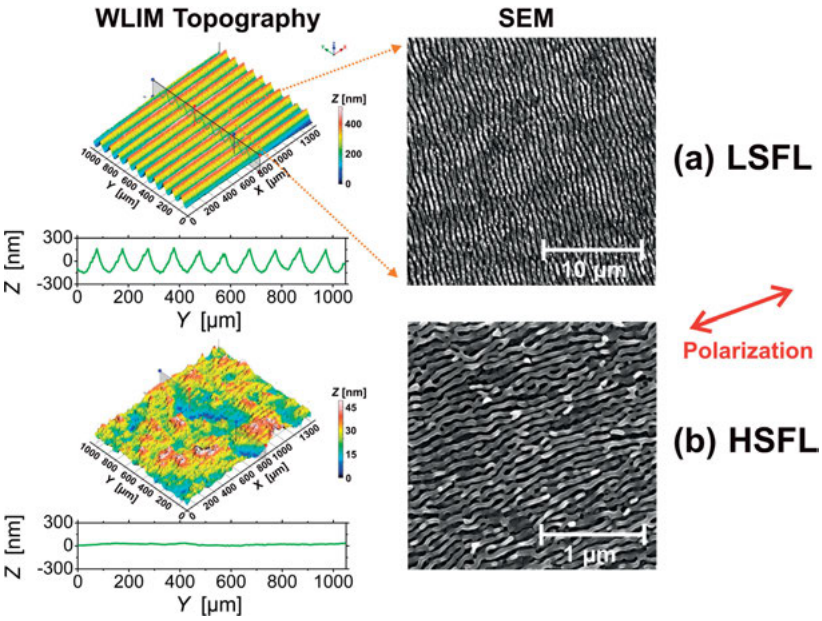

Fig. 7.2: White light interference microscopic topography (left) and scanning electron micrographs (right) from the centre of the fs-laser processed Ti6Al4V titanium alloy surface area (τ = 30 fs, λ = 800 nm, ν = 1 kHz). The processing conditions in (a) were optimized for the generation of LSFL (ϕ_0 = 0.11 J/cm^2, N_{eff} ~ 56, one pass) and in (b) for the generation of HSFL (ϕ_0 = 0.08 J/cm^2, N_{eff} ~ 280, two passes). The red double arrows indicate the direction of laser beam polarization. Note the different magnifications of the SEM images.

perpendicular to the polarization. Typical LSFL modulation depths were estimated by atomic force microscopy measurements to be (110 ± 20) nm.

On titanium surfaces (Ti, Ti6Al4V) HSFL were successfully generated with two processing passes at a lowered peak fluence of ϕ_0 = 0.08 J/cm^2 with a decreased scan velocity of v_x = 1 mm/s (N_{eff} ~ 280) and a reduced line offset of Δy = 0.05 mm. The corresponding WLIM topography (Fig. 7.2 (b), left) exhibits surface height variations of Δz = ±15 nm which are similar to those of the non-irradiated surface. However, the high-resolution SEM micrograph in the right part of the figure indicates HSFL with periodicities of (80±20) nm and an orientation parallel to the laser beam polarization. Atomic force microscopy measurements revealed typical HSFL modulation depths of (25 ± 10) nm.

It is instructive to evaluate the "photonic costs" (PC) for fs-laser nanostructuring in order to compare them to those of alternative industrial techniques. An estimation of the PC for the large area fs-laser fabrication of LIPSS using current state-of-the-art processing technology yields a typical value of 0.1 €/cm^2 for LSFL on metal surfaces [36].

7.3.2 Tribological characterization of LIPSS

On all four metals, the tribological performance of the LIPSS was evaluated by RSTT using paraffin oil (free of additives) and fully formulated engine oil as lubricants [34, 36]. The friction coefficient and the resulting wear tracks were characterized for sliding directions parallel and perpendicular to the ablation lines. No significant differences were found for sliding both directions, indicating that the directional effect due to the LIPSS is smaller than the uncertainty of the measurements. Hence, below we only present data for the sliding direction parallel to the laser processing lines.

The LIPSS (LSFL) covered steel samples (100Cr6, X30CrMoN15-1) generally showed an almost constant friction coefficient ranging between 0.11 and 0.17 in both lubricants (100Cr6: see [34]; X30CrMoN15-1: see [36]). These values were always very similar to the behavior of the non-processed surfaces and are typical for the regime between "mixed friction" (where both solid body friction and fluid friction appear; including solid asperity interaction) and "boundary friction" (where a direct contact between the sliding bodies is present) [41]. The wear tracks generated in engine oil were somewhat smaller than those obtained in paraffin oil. On 100Cr6 steel the LIPSS partly endured the RSTT [36].

The tribological performance of the two different LIPSS covered titanium materials (Ti, Ti6Al4V) was very similar but disparate from that of the steel materials. These findings are exemplified in detail for LSFL and HSFL in the following two sub-sections for the titanium alloy Ti6Al4V, complemented by a summary of the tribological performance of all four materials.

LSFL

Figure 7.3 contrasts the tribological performance of LSFL covered titanium alloy surfaces tested in paraffin oil [Fig. 7.3 (a), upper part] and in engine oil [Fig. 7.3 (b), lower part]. For each lubricant, the friction coefficient is shown vs. the number of sliding cycles (left). The corresponding wear tracks were imaged by OM (middle) and SEM (right). Additionally, the results of a non-irradiated reference sample location are provided for comparison.

In paraffin oil (Fig. 7.3 (a)), the friction coefficient of the LSFL covered titanium alloy surface and the reference area both exhibit large oscillations between 0.15 and 0.6. The inspection of the wear tracks by OM and SEM reveals severe damage in both tribologically tested regions (LSFL: lower row, reference: upper row). The LSFL were completely destroyed during the RSTT procedure.

In engine oil (Fig. 7.3 (b)), the friction coefficient of the reference area also shows rather large variations between ~ 0.3 and ~ 0.5, associated with a damaged surface region (see the OM and SEM images). Interestingly, on the LSFL covered surface, the friction coefficient is reduced by a factor of more than two and lies in the range of 0.11

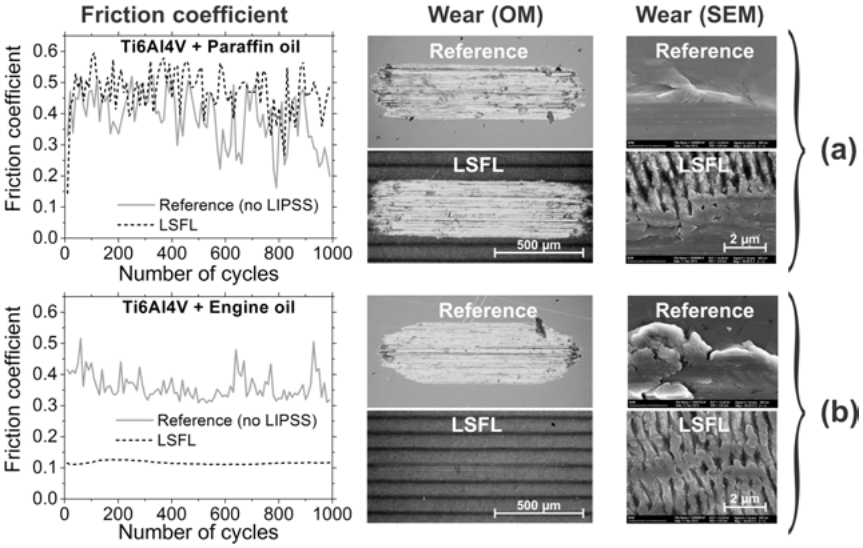

Fig. 7.3: Friction coefficient vs. number of sliding cycles (left) and the corresponding wear tracks of the LSFL covered Ti6Al4V titanium alloy surface tested in paraffin oil (a) and in engine oil (b). The middle column provides low-resolution optical micrographs, while the right column indicates high-resolution scanning electron micrographs. A reference measurement on the non-irradiated surface is provided for comparison.

to 0.13, without any oscillations. The complementing high-resolution SEM images reveal that the LSFL endured the tribological test (see lower right part of Fig. 7.3 (b)).

This very positive effect of the engine oil on the tribological performance of LSFL covered titanium surfaces was first reported in [34]. As the main differences between the two lubricants are the additives contained in the engine oil, the effect has been attributed to the presence of the additives. These additives efficiently cover and bond to the laser-generated surface structures and reduce friction and wear by forming a gliding intermediate layer which protects the sample from a direct intermetallic contact [36]. A chemical analysis of the additives contained in the engine oil used here revealed the presence of the elements calcium (3538 ppm), zinc (883 ppm), and phosphorous (836 ppm). The beneficial tribological influence of the additives might additionally be promoted by laser-induced oxidation in the ambient atmosphere at the highly reactive titanium surface. This laser-induced surface oxidation was indicated in preliminary energy dispersive x-ray analyses (EDX). However, it must be underlined that the positive tribological effect is observed only for the joint action of laser processing (LSFL) and in the presence of the engine oil additives. Simple laser-induced surface hardening or oxidation effects can be ruled out here, as the effect was not observed in paraffin oil (free of additives).

HSFL

Analogous tribological tests were performed on titanium alloy surfaces covered by sub-100 nm laser-induced nanostructures (HSFL). The results are compiled in Fig. 7.4. In both lubricants large friction coefficients were observed, oscillating between 0.15 and 0.6, along with significant damage of the surface within the wear tracks (see the OM and SEM images). The HSFL do not improve the tribological performance (in contrast to the LSFL with engine oil). Supposedly, this is related to the reduced laser processing fluence which affects the superficial oxidation. Moreover, the HSFL modulation depth of a few tens of nanometers is significantly smaller than the elastic deformation depth of ~ 300 nm estimated by the HDM for titanium. Hence, we assume that the HSFL are less beneficial for the tribological performance (in both lubricants).

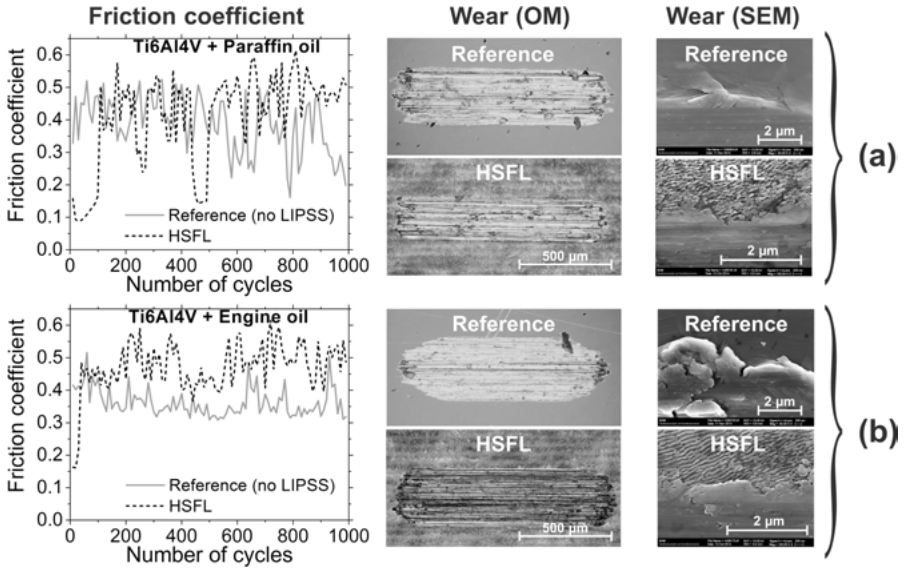

Fig. 7.4: Friction coefficient vs. number of sliding cycles (left) and the corresponding wear tracks of the HSFL covered Ti6Al4V titanium alloy surface tested in paraffin oil (a) and in engine oil (b). The middle column provides low-resolution optical micrographs, while the right column indicates high-resolution scanning electron micrographs. A reference measurement on the non-irradiated surface is provided for comparison.

Comparison of the materials

Table 7.1 summarizes the results of the RSTT performed for all four materials in paraffin oil and engine oil. The third column unites the measurements of the friction coefficient and indicates the upper and lower limits during the 1000 sliding cycles. The fourth column qualifies the wear behavior of the laser-nanostructured surfaces in comparison to the non-irradiated reference surface.

Tab. 7.1: Summary of the friction coefficient range and the wear behavior for the RSTT on four different materials and in two different lubricants. The wear column compares the wear track appearance with the corresponding reference track. Symbols and abbreviations: "–": more wear; "0", similar wear; "+": less wear; "++": significantly less wear.

Material	Lubricant	Friction coefficient [during 1000 cycles]	Wear [after 1000 cycles]	Literature
100Cr6	Paraffin oil	LSFL: 0.13–0.17	0	[34]
		HSFL not observed		
		Reference: 0.13–0.17		[34]
	Engine oil	LSFL: 0.13–0.17	0/+	[34]
		HSFL not observed		
		Reference: 0.13–0.17		[34]
X30CrMoN15-1	Paraffin oil	LSFL: 0.13–0.17	0	[36]
		HSFL not observed		
		Reference: 0.13–0.17		[36]
	Engine oil	LSFL: 0.11–0.14	0/+	[36]
		HSFL not observed		
		Reference: 0.11–0.14		[36]
Ti	Paraffin oil	LSFL: 0.12–0.65	–	[36]
		HSFL: 0.13–0.73	–	
		Reference: 0.12–0.55		[36]
	Engine oil	LSFL: 0.12–0.14	++	[36], this work
		HSFL: 0.15–0.75	–	
		Reference: 0.32–0.61		[36], this work
Ti6Al4V	Paraffin oil	LSFL: 0.14–0.6	–	[34], this work
		HSFL: 0.1–0.6	–	This work
		Reference: 0.16–0.6		[34], this work
	Engine oil	LSFL: 0.11–0.13	++	[34], this work
		HSFL: 0.15–0.6	–	This work
		Reference: 0.32–0.52		[34], this work

For both titanium materials (Ti and Ti6Al4V), the tribological performance of the surfaces with LSFL is superior in engine oil as lubricant (compared to paraffin oil). Hence, the alloying elements Al and V have no significant influence on the RSTT. They cannot account for the beneficial tribological behavior.

Although the roughness of both steel materials (100Cr6 and X30CrMoN15-1) was very different (factor 5) there is no significant impact on the tribological behavior in engine oil when compared to the paraffin oil (see Tab. 7.1). The positive tribological influence of the LSFL (as observed for the titanium materials) is much less pronounced on steel surfaces.

The same set of RSTT experiments (four metals, two lubricating oils) was repeated at a reduced normal force of 0.5 N, i.e., at the lower force limit of the home-made tribometer. Those measurements confirmed the results obtained at 1.0 N and are thus not listed here.

7.3.3 Optimization by laser beam shaping

Using a spatially Gaussian laser beam in the ablative regime, the linewise sample processing typically leads to a comb-like micrometer-sized surface structure which is superimposed onto the LIPSS topography (see WLIM topography shown in Fig. 7.2 (a)). This microstructure can easily provide height variations of a few hundred nanometers, which may even exceed the typical LIPSS modulation depths.

One way to reduce the height variations due to linear laser scanning is via *spatial beam shaping*, transforming the Gaussian laser beam into a top hat distribution. The impact on the laser ablation result is illustrated in Fig. 7.5. When strongly absorbing materials (such as metals) are processed by a Gaussian laser beam, in regions where the ablation threshold (ϕ_{th}) is locally surpassed, the topography typically follows a parabolic profile [42]. As a result, height variations are caused across the ablation region (see Figs. 7.5 (a) and 7.2 (a)). This effect can be significantly reduced when using a top hat beam (see Fig. 7.5 (b)).

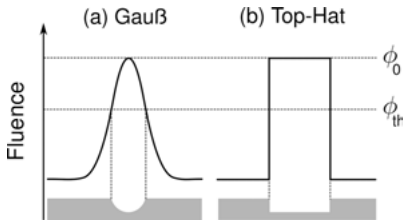

Fig. 7.5: Scheme of the laser processing with different spatially shaped beams (fluence profile and corresponding ablation topography). Gaussian laser beam (a), top hat laser beam (b).

In order to realize the spatial beam shaping experimentally (see setup illustrated in Fig. 7.6), the Ti:sapphire fs-laser pulses (800 nm, 80 fs, 100 Hz) were selected by an electromechanical shutter before passing through a programmable *spatial light modulator* (SLM) operated in reflection geometry (HOLOEYE PLUTO SLM, Berlin, Germany). The phase modulated (shaped) laser beam was then redirected by a mirror (M) and focused onto the sample surface by a spherical lens (L) with a focal length of 300 mm. A dielectric beam splitter (BS) and a CCD camera allowed the in situ monitoring of the laser beam profile in the focal region (sample surface). Using an adaptive beam shaping algorithm (Gerchberg-Saxton) [43, 44], the SLM was utilized to generate a top hat profile in the sample processing plane (see the example of the shaped beam profile in Fig. 7.6). The top hat-shaped beam profile is formed at the sample processing plane under optimized conditions by superposition and constructive interference of

the phase modulated partial waves. These waves are spatially selected and manipulated by beam shaping. In contrast to amplitude modulation techniques, laser pulse energy losses are reduced here. Upon meandering movement of the sample (motorized) under the spatially shaped top hat laser beam at a constant scan velocity and with an optimized line offset, square-shaped areas of $5 \times 5\,mm^2$ covered homogeneously by LIPSS were again processed in a single pass in air environment.

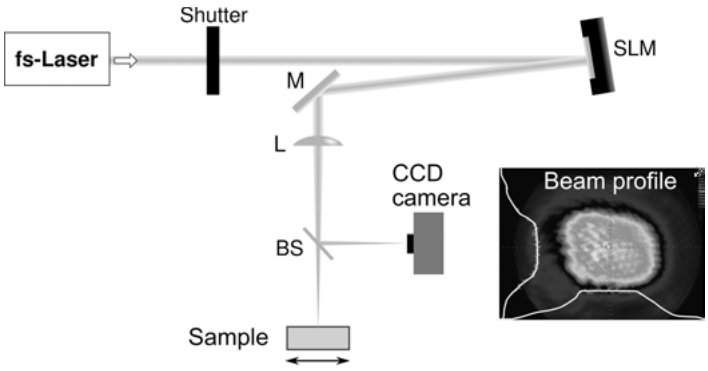

Fig. 7.6: Scheme of the experimental setup for laser processing with a top hat-shaped fs-laser beam. Abbreviations: SLM: spatial light modulator; M: mirror; L: lens; BS: beam splitter.

Figure 7.7 compares the WLIM surface topographies of a titanium surface processed with a Gaussian laser beam (a) and with a spatially shaped top hat beam (b), both with individually optimized processing conditions for the generation of LSFL. In both cases, SEM was used to confirm the homogeneous coverage of the surface by LSFL with periods around 600 nm. The laser treatment with a Gaussian beam shows periodic arrangement of individual ablation lines separated by 100 µm with height variations of ± 120 nm (see the cross-sectional line profile in the lower part of the Fig. 7.7 (a)). The residual surface height variations are reduced by a factor of 2–3 for processing with a spatially shaped top hat beam profile and account for less than ± 50 nm (see Fig. 7.7 (b)).

The tribological performance of the two titanium samples already shown in Fig. 7.7 was characterized by RSTT in engine oil. The results for the friction coefficient measured as function of the number of cycles are presented in Fig. 7.8 (a) for the sample processed with the Gaussian beam and in Fig. 7.8 (b) for the top hat-shaped beam treated specimen. In both cases, a reference measurement of the non-processed (polished) sample surface is added, which shows large friction coefficients between 0.3 and 0.6. In contrast, both fs-laser treated samples show very similar and almost constant friction coefficient values around 0.13 ± 0.01. However, direct comparison of the results indicates that the residual micrometer sized ablation line structures are not detrimental for the tribological performance here.

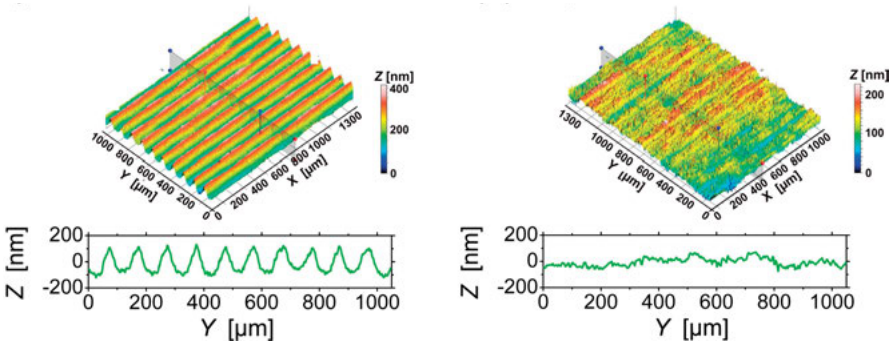

(a) Gauss (b) Top-Hat

Fig. 7.7: WLIM topography of the LSFL covered Ti surface processed under optimized conditions by a spatially Gaussian beam (a) and by a top hat laser beam (b).

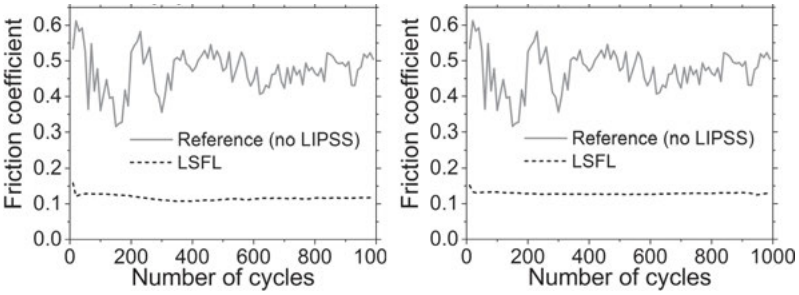

(a) Gauss (b) Top-Hat

Fig. 7.8: Friction coefficient vs. number of sliding cycles of the LSFL covered Ti surfaces previously characterized in Fig. 7.7 for a Gaussian (a) and a top hat laser beam (b). Both measurements were performed in engine oil.

7.4 Summary

Different types of LIPSS were homogeneously processed on $5 \times 5\,mm^2$ large surface areas on four different metals (two types of steel & two types of titanium materials). The respective surfaces were tribologically tested (reciprocal sliding against a 10 mm-100Cr6 ball: 1.0 N normal force, 1 mm stroke length, 1 Hz frequency, 1000 cycles) in two different lubricants (additive-free paraffin oil, and fully formulated engine oil) and the wear tracks were subsequently inspected. Under specific conditions (titanium material, engine oil), the nanostructures (LSFL) endured the tribological test and provided significantly reduced friction coefficients and almost no wear when compared to the non-irradiated (polished) surfaces. The effect in the nanostructured areas was attributed to additives contained in the engine oil forming a gliding interlayer preventing intermetallic contact, and might additionally be promoted by laser-induced

superficial oxidation. The presence of individual ablation lines after processing with a spatially Gaussian laser beam did not significantly affect the tribological performance. Sub-100 nm structures (HSFL) did not show a reduction of the friction coefficient. On steel surfaces the positive tribological impact of the LSFL is much less pronounced.

Acknowlegments

The authors would like to thank N. Slachciak (BAM 6.3) for help with the tribological tests, S. Benemann (BAM 6.8) and M. Tischer (MBI) for SEM characterizations, M. Weise (BAM 6.7) for WLIM measurements, and S. Binkowski and M. Scheibe (both BAM 6.3) for polishing titanium samples. The help of Dr. A. Mermillod-Blondin (MBI) in setting up the SLM is gratefully acknowledged. This work was supported by the German Science Foundation (DFG) under grant nos. RO 2074/7-2 and KR 3638/1-2.

References

[1] Birnbaum M. Semiconductor surface damage produced by ruby lasers. J Appl Phys 1965, 36, 3688–3689.
[2] van Driel HM, Sipe JE, Young JF. Laser-induced periodic surface-structure on solids – a universal phenomenon. Phys Rev Lett 1982, 49, 1955–1958.
[3] Bonse J, Krüger J, Höhm S, Rosenfeld A. Femtosecond laser-induced periodic surface structures. J Laser Appl 2012, 24, 042006.
[4] Costache F, Henyk M, Reif J. Surface patterning on insulators upon femtosecond laser ablation. Appl Surf Sci 2003, 208–209, 486–491.
[5] Huang M, Zhao F, Cheng Y, Xu N, Xu Z. Origin of laser-induced near-subwavelength ripples: interference between surface plasmons and incident laser. ACS Nano 2009, 3, 4062–4070.
[6] Obara G, Maeda N, Miyanishi T, Terakawa M, Nedyalkov NN, Obara M. Plasmonic and Mie scattering control of far-field interference for regular ripple formation on various material substrates. Opt Express 2011, 19, 19093–19103.
[7] Skolski JZP, Römer GRBE, Obona JV, Ocelik V, Huis in't Veld AJ, De Hosson JTM. Laser-induced periodic surface structures: fingerprints of light localization. Phys Rev B 2012, 85, 075320.
[8] Tsibidis GD, Barberoglou M, Loukakos PA, Stratakis E, Fotakis C. Dynamics of ripple formation on silicon surfaces by ultrashort laser pulses in subablation conditions. Phys Rev B 2012, 86, 115316.
[9] Höhm S, Rosenfeld A, Krüger J, Bonse J. Femtosecond diffraction dynamics of laser-induced periodic surface structures on fused silica. Appl Phys Lett 2013, 102, 054102.
[10] Derrien TJY, Krüger J, Itina TE, Höhm S, Rosenfeld A, Bonse J. Rippled area formed by surface plasmon polaritons upon femtosecond double-pulse irradiation of silicon: the role of carrier generation and relaxation processes. Appl Phys A 2014, 117, 77–81.
[11] Borowiec A, Haugen HK. Subwavelength ripple formation on the surfaces of compound semiconductors irradiated with femtosecond laser pulses. Appl Phys Lett 2003, 82, 4462.
[12] Bonse J, Munz M, Sturm H. Structure formation on the surface of indium phosphide irradiated by femtosecond laser pulses. J Appl Phys 2005, 97, 013538.

[13] Vorobyev AY, Makin VS, Guo C. Periodic ordering of random surface nanostructures induced by femtosecond laser pulses on metals. J Appl Phys 2007, 101, 034903.
[14] Bonse J, Rosenfeld A, Krüger J. On the role of surface plasmon polaritons in the formation of laser-induced periodic surface structures upon irradiation of silicon by femtosecond-laser pulses. J Appl Phys 2009, 106, 104910.
[15] Sipe JE, Young JF, Preston JS, van Driel HM. Laser-induced periodic surface structure. I. Theory. Phys Rev B 1983, 27, 1141–1154.
[16] Bonch-Bruevich AM, Libenson MN, Makin VS, Trubaev VV. Surface electromagnetic-waves in optics. Opt Eng 1982, 31, 718–730.
[17] Dufft D, Rosenfeld A, Das SK, Grunwald R, Bonse J. Femtosecond laser-induced periodic surface structures revisited: A comparative study on ZnO. J Appl Phys 2009, 105, 034908.
[18] Martsinowskii GA, Shandybina GD, Smirnov DS, Zabotnov SV et al. Ultrashort excitations of surface polaritons and waveguide modes in semiconductors. Opt Spectroscop 2008, 105, 67–72.
[19] Straub M, Afshar M, Feili D, Seidel H, König K. Surface plasmon polariton model of high-spatial frequency laser-induced periodic surface structure generation in silicon. J Appl Phys 2012, 111, 124315.
[20] Derrien TJY, Koter R, Krüger J, Höhm S, Rosenfeld A, Bonse J. Plasmonic formation mechanism of periodic 100-nm-structures upon femtosecond laser irradiation of silicon in water. J Appl Phys 2014, 116, 074902.
[21] Vorobyev AY, Guo C. Colorizing metals with femtosecond laser pulses. Appl Phys Lett 2008, 92, 041914.
[22] Dusser B, Sagan Z, Soder H, Faure N, Colombier JP, Jourlin M, Audouard E. Controlled nanostructures formation by ultrafast laser pulses for color marking applications. Opt Express 2010, 18, 2913–2924.
[23] Groenendijk MNW, Meijer J. Surface microstructures obtained by femtosecond laser pulses. CIRP Annals 2006, 55, 183–186.
[24] Qi L, Nishii K, Namba Y. Regular subwavelength surface structures induced by femtosecond laser pulses on stainless steel. Opt Lett 2009, 34, 1846–1848.
[25] Hou S, Huo Y, Xiong P et al. Formation of long- and short-periodic nanoripples on stainless steel irradiated by femtosecond laser pulses. J Phys D: Appl Phys 2011, 44, 505401.
[26] Bonse J, Höhm S, Rosenfeld A, Krüger J. Sub-100 nm laser-induced periodic surface structures upon irradiation of titanium by Ti:sapphire femtosecond laser pulses in air. Appl Phys A 2013, 110, 547–551.
[27] Zorba V, Stratakis E, Barberoglou M, Spanakis E, Tzanetakis P, Fotakis C. Tailoring the wetting response of silicon surfaces via fs structuring. Appl Phys A 2008, 93, 819–825.
[28] Mizuno A, Honda T, Kiuchi J, Iwai Y, Yasumaru N, Miyazaki K. Friction properties of the DLC film with periodic structures in nano-scale. Tribol Online 2006, 1, 44–48.
[29] Yasumaru N, Miyazaki K, Kiuchi J. Control of tribological properties of diamond-like carbon films with femtosecond-laser-induced nanostructuring. Appl Surf Sci 2008, 254, 2364–2368.
[30] Yasumaru N, Miyazaki K, Kiuchi J, Sentoku E. Frictional properties of diamond-like carbon, glassy carbon and nitrides with femtoseond-laser-induced nanostructure. Diamond Relat Mater 2011, 20, 542–545.
[31] Pfeiffer M, Engel A, Gruettner H, Guenther K, Marquardt F, Reisse G, Weissmantel S. Ripple formation in various metals and super-hard tetrahedral amorphous carbon films in consequence of femtosecond laser irradiation. Appl Phys A, 2013, 110, 655–659.
[32] Eichstädt J, Römer GRBE, Huis in't Veld AJ. Towards friction control using laser-induced periodic surface structures. Phys Procedia 2012, 12, 7–15.

[33] Chen CY, Chung CJ, Wu BH et al. Microstructure and lubricating property of ultra-fast laser pulse textured silicon carbide seals. Appl Phys A 2012, 107, 345–350.
[34] Bonse J, Koter R, Hartelt M, Spaltmann D, Pentzien S, Höhm S, Rosenfeld A, Krüger J. Femtosecond laser-induced periodic surface structures on steel and titanium alloy for tribological applications. Appl Phys A 2014, 117, 103–110.
[35] Sawada Y, Sawada H, Hirayama T, Tomita N. Tribological performance of femtosecond laser-induced periodic surface structures, J Bone Joint Surg Br 2012, 94-B, 161
[36] Bonse J, Koter R, Hartelt M, Spaltmann D, Pentzien S, Höhm S, Rosenfeld A, Krüger J. Femtosecond laser-induced periodic surface structures on titanium and a high toughness bearing steel. Appl Surf Sci 2014, http://dx.doi.org.10.1016./j.apsusc.2014.08.111, in press.
[37] Bonse J, Mann G, Krüger J, Marcinkowski M, Eberstein M. Femtosecond laser-induced removal of silicon nitride layers from doped and textured silicon wafers used in photovoltaics. Thin Solid Films 2013, 542, 420–425.
[38] Fouvry S, Paulin C. An effective friction energy density approach to predict solid lubricant friction endurance: Application to fretting wear. Wear 2014, 319, 211–226.
[39] Meine K, Schneider T, Spaltmann D, Santner E. The influence of roughness on friction – Part I: The influence of a single step. Wear 2002, 253, 725–732.
[40] Meine K, Schneider T, Spaltmann D, Santner E. The influence of roughness on friction – Part II: The influence of multiple steps. Wear 2002, 253, 733–738.
[41] Czichos H, Habig KH. Tribologie-Handbuch: Tribometrie, Tribomaterialien, Tribotechnik. 3rd ed. Wiesbaden, Germany, Teubner-Vieweg Verlag, 2010.
[42] Bonse J. All-optical characterization of single femtosecond laser-pulse-induced amorphization in silicon. Appl Phys A 2006, 84, 63–66.
[43] Gerchberg RW, Saxton WO. A practical algorithm for the determination of phase from image and diffraction plane pictures. Optik 1972, 35, 237–241.
[44] Sanner N, Hout N, Audouard E, Larat C, Huignard JP, Loiseaux B. Programmable focal spot shaping of amplified femtosecond laser pulses. Opt Lett 2005, 30, 1479–1481.